

Bayesian Analysis for Remote Biosignature Identification on exoEarths (BARBIE) III: Introducing the KEN

NATASHA LATOUF,^{1,2,3,*} MICHAEL D. HIMES,^{4,5,2} AVI M. MANDELL,^{2,3} MICHAEL DANE MOORE,^{6,7,8} VINCENT KOFMAN,^{2,3,9}
GERONIMO L. VILLANUEVA,^{2,3} AND CHRIS STARK^{2,3}

¹*Department of Physics and Astronomy, George Mason University, 4400 University Drive MS 3F3, Fairfax, VA, 22030, USA*

²*NASA Goddard Space Flight Center, 8800 Greenbelt Road, Greenbelt, MD 20771, USA*

³*Sellers Exoplanets Environment Collaboration, 8800 Greenbelt Road, Greenbelt, MD 20771, USA*

⁴*NASA Postdoctoral Program Fellow, NASA Goddard Space Flight Center, 8800 Greenbelt Road, Greenbelt, MD 20771, USA*

⁵*Morgan State University, 1700 E Cold Spring Lane, Baltimore, MD 21251, USA*

⁶*NASA Goddard Space Flight Center, Greenbelt, MD, USA.*

⁷*Business Integra, Inc., Bethesda, MD, USA.*

⁸*Sellers Exoplanets Environment Collaboration, 8800 Greenbelt Road, Greenbelt, MD 20771, USA*

⁹*Integrated Space Science and Technology Institute, Department of Physics, American University, Washington DC*

ABSTRACT

We deploy a newly-generated set of geometric albedo spectral grids to examine the detectability of methane (CH₄) in the reflected-light spectrum of an Earth-like exoplanet at visible and near-infrared wavelengths with a future exoplanet imaging mission. By quantifying the detectability as a function of signal-to-noise ratio (SNR) and molecular abundance, we can constrain the best methods of detection with the high-contrast space-based coronagraphy slated for the next generation telescopes such as the Habitable Worlds Observatory (HWO). We used 25 bandpasses between 0.8 and 1.5 μm . The abundances range from a modern-Earth level to an Archean-Earth level, driven by abundances found in available literature. We constrain the optimal 20%, 30%, and 40% bandpasses based on the effective SNR of the data, and investigate the impact of spectral confusion between CH₄ and H₂O on the detectability of each one. We find that a modern-Earth level of CH₄ is not detectable, while an Archean Earth level of CH₄ would be detectable at all SNRs and bandpass widths. Crucially, we find that CH₄ detectability is inversely correlated with H₂O abundance, with required SNR increasing as H₂O abundance increases, while H₂O detectability depends on CH₄ abundance and selected observational wavelength, implying that any science requirements for the characterization of Earth-like planet atmospheres in the VIS/NIR should consider the abundances of both species in tandem.

Keywords: planetary atmospheres, telescopes, methods: numerical; techniques: nested sampling, grids

1. INTRODUCTION

The Habitable Worlds Observatory (HWO), recommended by the [National Academies of Sciences, Engineering, and Medicine \(2021\)](#), is slated to launch in the 2040s with the foundational goal of constraining the properties of Earth-like exoplanets using high-contrast

imaging. This type of imaging is one of the first steps on the path to determining planet habitability for potentially Earth-like worlds and providing context for the development of our own Earth through time. The [National Academies of Sciences, Engineering, and Medicine \(2021\)](#) identified a primary science driver to detect and characterize 25 exoEarth candidates (EECs) in the habitable zones (HZ) of nearby stars. Characterization of an exoplanet's atmosphere can provide vital information on the formation, history, and physical composition of the planet; for potentially habitable planets, we can also search their atmospheres for biosignatures that can hint

Corresponding author: Natasha Latouf
nlatouf@gmu.edu, natasha.m.latouf@nasa.gov

* NSF Graduate Research Fellow, 2415 Eisenhower Ave, Alexandria, VA 22314

at the likelihood of clement conditions and biological activity (Schwieterman et al. 2018). A holistic understanding of robust biological indicators and necessary signal-to-noise ratio (SNR) for detection is crucial to establishing an efficient observing procedure and driving instrument development for HWO.

With the advances in high-contrast imaging instrumentation planned for HWO (The LUVOIR Team 2019), the ability to detect flux from a habitable Earth-twin is becoming a realistic possibility, which can unlock new molecular detections. Previous works, such as Feng et al. (2018); Damiano et al. (2023), and Young et al. (2024), have investigated biosignature detectability at varying wavelengths, such as O₃ in the UV, and found that detectability is drastically effected by the chosen observational wavelength. There are many molecules that peak in their absorption outside of the optical region, and would thus require a more thorough investigation of required resolving power and abundance for detection.

Methane (CH₄) shows absorption in the visible and NIR wavelength regimes, with a range of spectral features varying in optical depth. Other molecules such as O₂ and O₃ can have abiotic production mechanisms and thus may not necessarily indicate a biosignature Schindler & Kasting (2000); Domagal-Goldman et al. (2014). Even if from biotic sources, many eras of early Earth had extremely low levels of O₂, such as the Proterozoic, leading to a very unlikely or impossible chance of detection Planavsky et al. (2014); Latouf et al. (2024). However, in low-O₂ eras of Earth, it is possible that the atmosphere was instead CH₄-rich, such as in the Archean era, and thus CH₄ would be readily detectable Arney et al. (2016); Wogan et al. (2020). Further, CH₄ has a very short lifetime in Earth’s atmosphere when only produced by abiogenic sources due to destruction by oxygen, and thus a detection of a high CH₄ abundance would strongly indicate biogenic sources as well as abiogenic (Krissansen-Totton et al. 2018; Wogan et al. 2020). Enabling a detection of CH₄ can increase the likelihood of confirming an Earth-twin discovery.

In this work, we use the spectral grid-based Bayesian inference method first described in Susemihl et al. (hereafter S23 2023), and used in Latouf et al. (hereafter BARBIE1 2023) and Latouf et al. (hereafter BARBIE2 2024). In this method, 1.4 million geometric albedo spectra at discrete parameter values are generated, and forward models for Bayesian retrievals are then interpolated from the grid. However, the S23 grid has a limited wavelength range, operating primarily at optical wavelengths (0.5–1 μm), and consists of six varied parameters: surface pressure (P₀), surface albedo (A_s),

and gravity (g), H₂O, O₂, and O₃. However, the limited set of atmospheric constituents bounded the applicability of the S23 grid to oxygen-rich atmospheric compositions at visible wavelengths (0.4 - 1.0), and necessitated new grids to explore new wavelength ranges and atmospheric compositions. Figure 1 portrays a representative spectrum for an Earth-twin in the top panel, and every molecule and their absorbance across the full spectral range of the new grids (0.2–2 μm) in the bottom panel. By focusing only on the visible, many molecular species are not considered, including key biosignatures such as CH₄ and CO₂. By building new grids with larger wavelength coverage and more parameters, we can further investigate the optimization of exoplanet characterization observations and build a more robust observing strategy for biosignatures.

This project is a direct continuation from BARBIE1 and BARBIE2, and in this paper we extend the same methodology to validate our new grids and study the impact of longer wavelengths (i.e. into the NIR) with CH₄. In [§] 2 we present the methodology of our grid-building, validation, and simulations, also providing a brief summary of BARBIE1 and BARBIE2. In [§] 3 we present the results of our simulations for modern and varying abundances of CH₄, as well as an analysis of how CH₄ and H₂O detectability affect one another. In [§] 4 we discuss the presented results and analyze the impact for future observations of varying Earth-twin epochs as a function of wavelength and further bandpass widths. In [§] 5 we present our conclusions and ideas for future work.

2. METHODOLOGY

2.1. A New Grid-Building Scheme

Although spectral retrieval studies have been used extensively to explore the detectability of atmospheric compositions for the direct imaging of exoplanets for multiple telescopes both current and future (e.g., Lupu et al. 2016; Nayak et al. 2017; Smith et al. 2020; Damiano & Hu 2022; Young et al. 2024), these retrievals are extremely computationally expensive. Most Bayesian retrievals use real-time radiative transfer calculations, combined with exploring large parameter spaces, mission capabilities, and constant model improvement that increases computation time to a rate that is not easily usable. Different methods to accelerate retrievals have been explored through efficient radiative transfer schemes or machine learning (e.g., Robinson & Salvador 2023; Zingales & Waldmann 2018; Márquez-Neila et al. 2018; Cobb et al. 2019; Fisher et al. 2020; Himes et al. 2022).

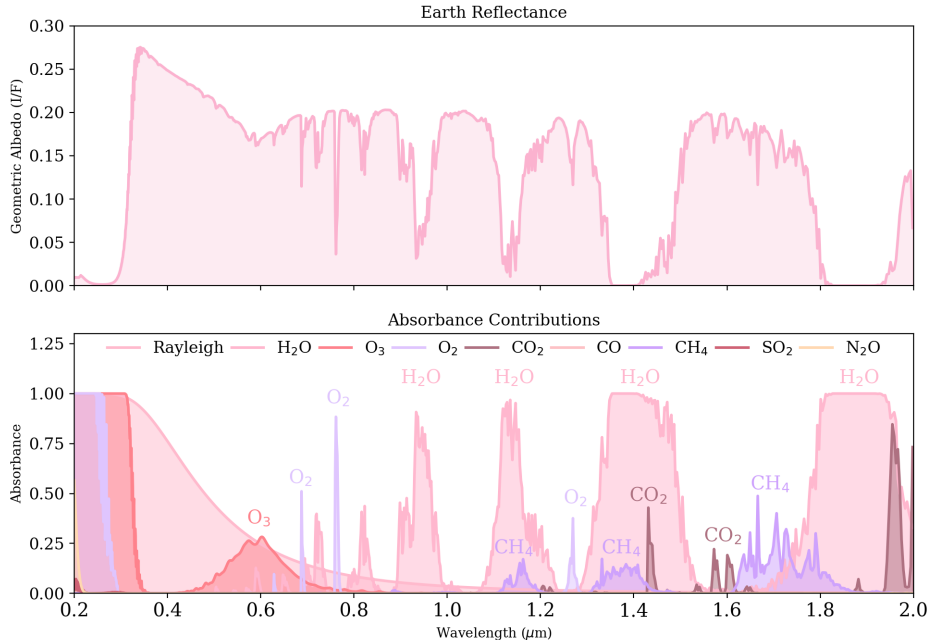
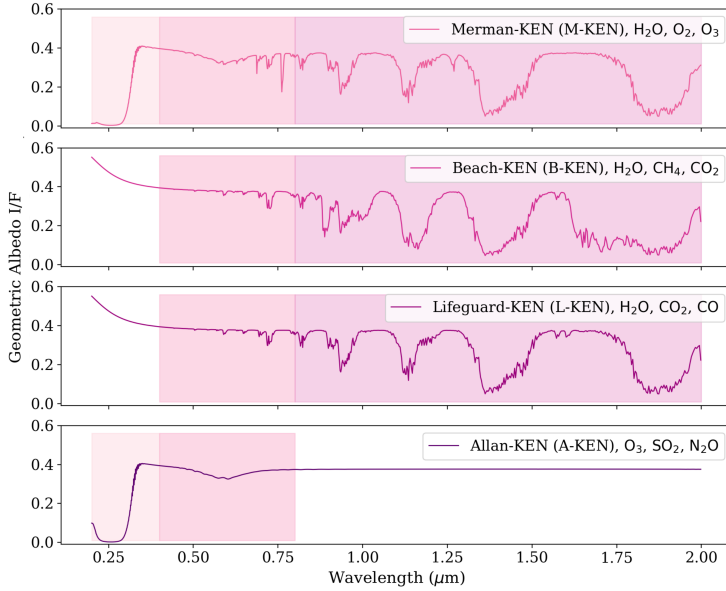


Figure 1. In the top panel, we present a representative spectrum from our work where molecular contributions are visible, with the y-axis representing the geometric albedo. In the bottom panel, we present the absorbance contributions of every molecule available in the KEN grids, as well as the Rayleigh scattering also included: H₂O, O₂, O₃, CH₄, CO, CO₂, SO₂, and N₂O, with the y-axis representing absorption. The x-axes are both the full wavelength range of the KEN grids (0.2–2 μm). Note that SO₂ and N₂O absorb at 0.2 μm very minimally, without features in other locations in this wavelength range.

In order to facilitate the efficient production of new optimized spectral grids for our grid-based retrievals, we developed a Python package called Gridder, which is a generalized grid-building scheme based on the methodology of S23 (Himes et al. in prep). Gridder produces arbitrary spectral grids using the Planetary Spectrum Generator, a publicly available radiative transfer model for creating planetary spectra (PSG, Villanueva et al. 2018, 2022). PSG can be used to calculate spectra over an ultra-broad wavelength range (50 nm to 100 mm) and includes planetary atmospheres, surfaces, and bulk properties such as aerosols, atomic, continuum, and molecular scattering/radiative processes implemented layer-by-layer. The Gridder parameter structure is highly customizable, allowing any input parameter to PSG to be used as a parameter in the optimized grid, including parameterized thermal profiles (e.g., isothermal, adiabatic, Line (2013)) and atmospheric chemistry (e.g., constant-with-altitude, thermochemical equilibrium). In addition to the error metric of S23, Gridder offers other common metrics, such as the maximum absolute percent error and mean squared error, for greater control over the resulting grid’s accuracy. Gridder features various optimizations (e.g., parallelization, checkpoints) to ensure efficient production of optimized spectral grids in a consistent, reproducible manner. Using Gridder, we have built a new set of spectral grids, each with six param-

eters to decrease grid-building computational time, but over a far wider wavelength range from the UV to NIR (0.2–2.0 μm), and we have added the additional molecular atmospheric constituents CH₄, CO₂, CO, SO₂, and N₂O.

Our newly built grid set, hereafter the KEN grids (no acronym; they’re just Ken), allow for a direct comparison between grids since they cover the same wavelength range and three base parameters of P_0 , A_s , and g with R_p fixed to $1 R_{\oplus}$. However, they reduce computational time by taking advantage of the different spectral regions covered by absorption features of different molecules. Any molecules that have overlapping spectral features (for the range of atmospheric pressures examined) are housed within the same grid, while any that are orthogonal to each other do not need to be simultaneously retrieved within one grid, such as CH₄ and O₃. The background gas in each grid is set to $N_2 = 1 - P_1 - P_2 - P_3$ where $P_1 - P_3$ are the molecules per grid. In this way, we can also investigate the effects of false positive or negative molecular detection due to overlapping features. We developed four different spectral grids at a resolving power of 500 ($R = 500$) which can then be binned to lower resolving powers, with the ability to vary the cloud fraction C_f at any value between 0% cloudy to 100% cloudy. We describe the molecular parameters in each named grid in the KEN grid set, along with



Grid Name	Parameter Symbol	Number of Points	Grid Min	Grid Max
Merman-KEN	H ₂ O	25	10 ⁻¹⁰	10 ^{-0.5}
	O ₃	13	10 ⁻¹⁰	10 ⁻⁵
	O ₂	14	10 ⁻¹⁰	10 ^{-0.001}
	P ₀	12	10 ⁻¹ bar	10 bar
	A _s	4	10 ⁻²	1
Beach-KEN	g	7	1 m/s ²	30 m/s ²
	H ₂ O	14	10 ⁻¹⁰	10 ^{-0.5}
	CH ₄	16	10 ⁻¹⁰	10 ^{-0.1}
	CO ₂	9	10 ⁻¹⁰	10 ⁻¹
	P ₀	9	10 ⁻¹ bar	10 bar
Lifeguard-KEN	A _s	4	10 ⁻²	1
	g	5	1 m/s ²	30 m/s ²
	H ₂ O	14	10 ⁻¹⁰	10 ^{-0.5}
	CO ₂	9	10 ⁻¹⁰	10 ⁻¹
	CO	6	10 ⁻¹⁰	10 ^{-0.001}
Allan-KEN	P ₀	9	10 ⁻¹ bar	10 bar
	A _s	4	10 ⁻²	1
	g	5	1 m/s ²	30 m/s ²
	N ₂ O	16	10 ⁻¹⁰	10 ^{-0.001}
	O ₃	20	10 ⁻¹⁰	10 ⁻⁵
	SO ₂	16	10 ⁻¹⁰	10 ^{-0.001}
	P ₀	11	10 ⁻¹ bar	10 bar
	A _s	5	10 ⁻²	1
	g	6	1 m/s ²	30 m/s ²

Figure 2. Herein we present a modern, 50% cloudy, Earth-like spectrum for each grid over the full wavelength range, to illustrate the absence and presence of each molecule per grid. Each legend shows the name of the grid along with the present molecular constituents, with geometric albedo on the y-axis and wavelength on the x-axis. The highlighted regions portray the UV, Visible, and NIR wavelength regions, and they are present in the grids that are most useful in said region. The table on the right contains the grid structure for all KEN grids (grid name, spacing, and number of points) for the clear grid versions. For the combined clear and cloudy grids, the overall size is doubled. It also includes the minimum and maximum values for each grid parameter.

a modern Earth-like spectrum per grid and the highlighted wavelength regimes for use per grid, in Figure 2.

The KEN grids will allow us to investigate varying atmospheric compositions beyond O₂-dominated atmospheres, such as CH₄ or CO₂ dominated, to develop observational procedures for multiple planetary archetypes through wavelength.

2.2. BARBIE Methodology

We follow an identical methodological approach to that of BARBIE1 and BARBIE2 for the CH₄ case study analysis. Herein we present a brief summary of the main steps in our analysis. For more detailed information, please see BARBIE1 and BARBIE2.

1. We set a modern-Earth twin as our fiducial data spectrum following Feng et al. (2018), with isotropic volume mixing ratios (VMRs) H₂O = 3 × 10⁻³, O₃ = 7 × 10⁻⁷, O₂ = 0.21, constant temperature profile at 250 K, A_s of 0.3, P₀ of 1 bar, and a planetary radius fixed at R_p = 1 R_⊕. We bin our grid from the native resolving power of 500 to 140 and 70 for our simulations, and split the spectrum in 25 evenly spaced bandpasses across 20%, 30%, and 40% widths. R = 140 is generally accepted in the optical regime, while R = 70 is generally accepted in the NIR (The LUVUOIR Team 2019). These ranges mimic the simultaneous bandpasses

that may be achieved with high-performance coronagraphs in the future, or dual coronagraphs that can be used in combination (Ruane et al. 2015; Por 2020; Juanola-Parramon et al. 2022).

2. We run a series of Bayesian nested sampling retrievals using PSGnest¹ housed in PSG. PSGnest is a Bayesian spectral retrieval methodology adapted from the original Fortran version of the Multinest retrieval algorithm (Feroz et al. 2009) and designed for application to exoplanetary observations (i.e. incorporating grid multi-dimensional interpolation, grid retrievals, the fitting methods, as well as the Multinest retrievals).
3. We receive the highest-likelihood values, the average values from the posterior distributions, uncertainties, and the log evidence (logZ) (Villanueva et al. 2022) as outputs. We then calculate the log-Bayes factor (lnB; Benneke & Seager 2013); this compares retrievals with and without a given molecule to estimate the likelihood of the molecule’s presence in the exoplanet’s atmosphere. For our purposes, lnB < 2.5 is unconstrained (no detection), 2.5 ≤ lnB < 5.0 is a weak detection,

¹ <https://psg.gsfc.nasa.gov/apps/psgnest.php>

CH ₄ (VMR)	Assumed Earth Epoch (Age)
1.65×10^{-6}	Hadean (3.9 Gyr)
1.65×10^{-3}	Archean (3.5 Gyr)
7.07×10^{-3}	Archean (2.4 Gyr)
1.65×10^{-3}	Proterozoic (2.0 Gyr)
4.15×10^{-4}	Phanerozoic (0.8 Gyr)
$1.65 \times 10^{-6 \dagger}$	Phanerozoic (0.3 Gyr) [†]

Table 1. The above values were used in our simulations for CH₄, moving from Earth-like values into different epochs of Earth’s history based on [Kasting \(2005\)](#) and [Kaltenegger et al. \(2007\)](#), and interpolating to provide more points between large gaps of abundance.

[†] Modern Earth-like value.

and $\ln B \geq 5.0$ is a strong detection (see Table 2 of [Benneke & Seager 2013](#)). We also calculate the median, upper, and lower limit values of the 68% credible region ([Harrington et al. 2022](#)). However $\ln B$ is a better estimation of detection rather than the 68% credible region since it is directly investigating the molecular presence vs absence and calculating which iteration yields the best fit, while the 68% credible region, by definition, includes the true value 68% of the time. $\ln B$ is not calculated for non-gaseous components, since those factors cannot be absent.

This process is then repeated for varying abundances. For this work, we vary CH₄ according to Table 1, following [Kasting \(2005\)](#) and [Kaltenegger et al. \(2007\)](#), while also adding values to bridge the large gap between abundance values (i.e., between Hadean and Archean values). The level of CH₄ present in any specific habitable exoplanet atmosphere is uncertain, since CH₄ production is significantly driven by biological activity; the same is true for any other biologically-produced species. Since we are not running fully physically-consistent chemistry models, we therefore use modern-Earth values as the default for other species as well as to isolate the effect of a single molecule, as in prior BARBIE works. We also investigate the effects of H₂O on CH₄ detectability by testing a range of combined H₂O and CH₄ values, shown in Table 2. All retrievals were performed between 0.8 and 1.5 μm with 20%, 30%, and 40% bandpass widths, and $R=140$ and $R=70$. We carefully select a narrower wavelength range in order to investigate the detectability of CH₄ in the optical or at the critical 0.9 μm H₂O feature; this is currently poised as the first step in observations following the decision tree technique in [Young et al. \(2024\)](#).

3. RESULTS

3.1. Grid Validation

In S23 Figure 8, they investigate the interpolation error in the developed grid to ensure that the grid is not introducing large error past any known interpolation error. We have replicated this in Figure 3 using the same technique as in S23 using our M-KEN grid, as that has the same parameters as in the S23 grid. To summarize, we ran 6D retrievals for each value of each parameter in the test grid. The test grid in use consists of the midpoint values of the M-KEN grid as interpolation error is typically maximized near the midpoints, and thus to test the error we want to investigate the area of highest error. For each parameter set, a “true” spectrum was created (i.e., pulling the data spectrum directly from the midpoints grid) at an SNR of 20. The retrievals were then repeated, but the data spectrum was created by interpolating from the main M-KEN grid (i.e., the way that all retrievals will work when using KEN grids with PSGnest). We use the offset between the values retrieved for the “true” and interpolated spectra to assess the impact of interpolation error on these retrievals.

Although the M-KEN grid covers a wider wavelength range than the S23 grid, Figure 3 covers the wavelength range of 0.4–1 μm in order to directly replicate the range in S23. The error from retrieving on interpolated data is shown in pink dots, while the error from retrieving on “true” data is shown in purple stars. We also calculate the 68% credible region and portray those as error bars. The left column shows the full extent of the offset for every point, while the right column zooms in to the regions shown in the black dotted lines. We select these areas based on where there is a high concentration of overlapping points. Any differences between the results are due to interpolation error.

We find that the retrieval error is generally very similar for both the “true” and interpolated data retrievals, with the derived retrieval error for both always within 1σ of the input value. The outlier errors, as in S23, are at small P_0 , and at large O_3 , although even those error ranges are no more than 15%. The average error hovers at below 5%, while the error between the interpolated and true data is never larger than 2% (with the singular exception of 10% at low O_3). In fact, our error spread is much smaller than S23, validating that the new optimization procedures of Gridder yield higher fidelity results with a much faster overall runtime. This confirms that the Gridder selection of grid points has been successful, with interpolation error not serving as a significant inhibitor for performing retrievals in this region.

To further isolate the impact of the retrieval error induced by interpolation within the grid apart from the

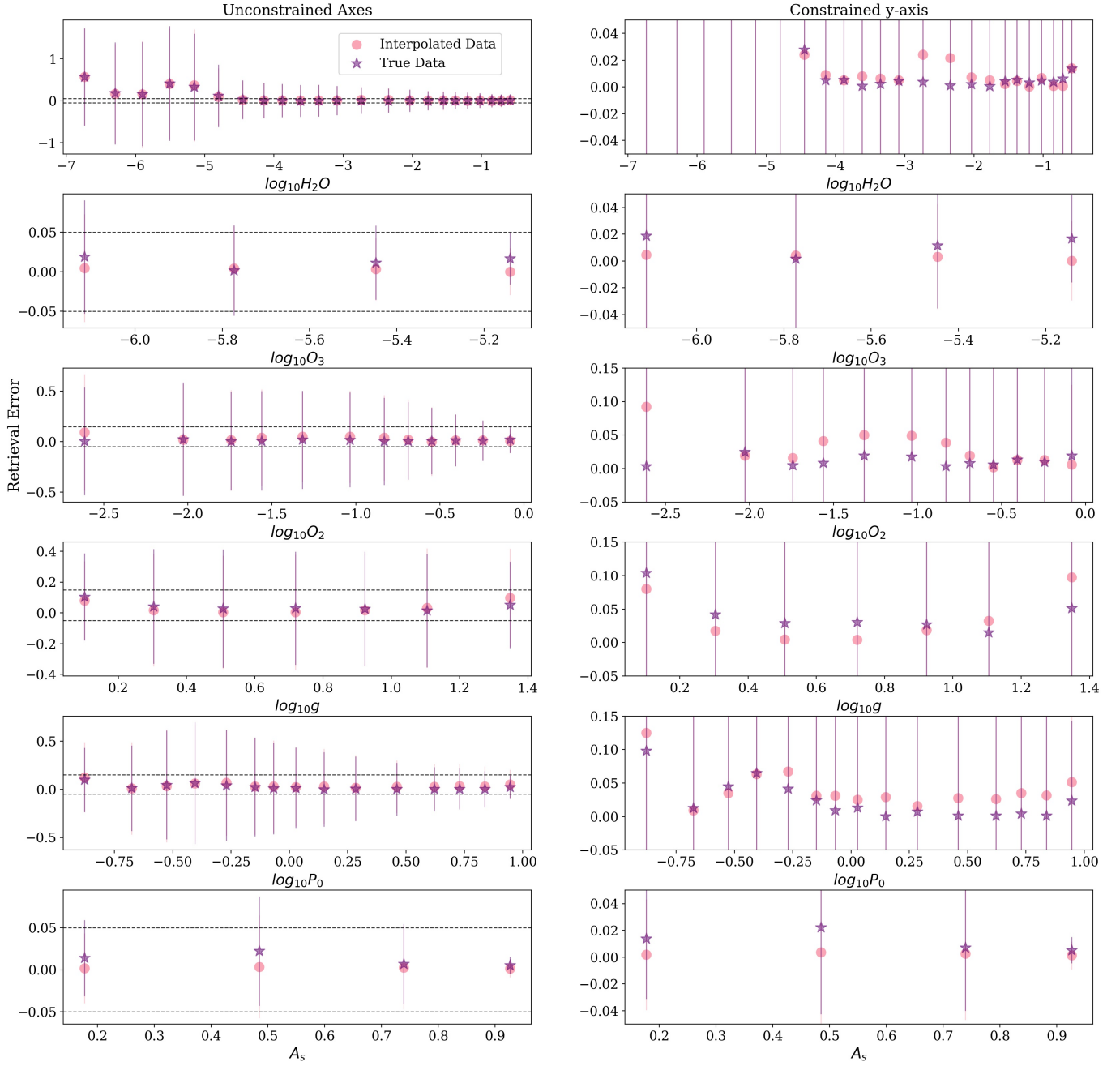


Figure 3. Interpolation error across a 6D retrieval across parameter space. The retrieval error is defined as the difference between the true and retrieved values. The pink dots represent retrievals performed on a spectrum interpolated from the KEN grid, and the purple stars represent retrievals performed on a PSG-calculated spectrum. The error bars on these points are drawn as the 68% credible regions. The left column shows the full y-axes, and the right column zooms in to the portion on the y-axes contained within the horizontal dashed black lines that cover the areas of lowest error.

Bayesian inference routine, we performed 4800 retrievals using the UltraNest package (Buchner 2016, 2019, 2021) on PSG-simulated spectra for values near the midpoints across the B-KEN grid’s parameter space. We use the grid’s native $R = 500$ spectral resolution and the full 0.2–2 μm wavelength range and assume a SNR of 15 for each wavelength channel. We find that the mean absolute error (MAE) between the maximum likelihood and the known true value is typically ~ 0.02 for A_s and ~ 0.2 for all other parameters when there is sufficient information content to constrain the parameter. This finding is generally consistent with Figure 3. When H_2O , CH_4 , and CO_2 can simultaneously be constrained, the MAE for the extrema of the 3σ region of all parameters is nearly equal to the MAE of the maximum likelihood, indicating that the 1D marginalized posteriors are offset from the known truth. This bias is generally negligible except in the case of g , where the mean absolute percentage error can be $> 60\%$ at low values of $\log_{10}g$ and $\sim 20\%$ for Earth-like gravities. These results represent worst-case scenarios; under typical grid usage conditions ($R = 140$, reduced wavelength coverage, at least one parameter not at a grid midpoints), these errors will be reduced.

We present another analysis of grid efficacy in Figure 4, looking specifically at the deep CH_4 feature centered at 1.1 μm . This presents modern-Earth values of all parameters except CH_4 , which is at an Archean value - increasing the CH_4 value is necessary to investigate grid efficacy, as we expect it to be well constrained. This is using the B-KEN grid, which is also the grid used for all the science cases explored in this work. The B-KEN grid is the only KEN grid that contains CH_4 , thus it is our only option to investigate CH_4 detectability. We find that there are no sharp cut-offs in our 1D histograms except for g , which can especially be seen in the 2D marginalized posterior for g and P_0 . However, g around the Earth value is the primary use case for these grids, which is well retrieved. CO_2 and g also have significant posterior density at 1×10^{-10} VMR and 1 m/s^2 respectively, indicating that the 68% credible region is underestimated. However, any molecule at such low abundances does effect spectral change, and CO_2 is unconstrained in this wavelength region where there is no CO_2 . We also see known and expected degeneracies with A_s and C_f , with every parameter, especially the molecular parameters, heavily impacted, but every parameter is also retrieved within the 68% credible region.

For further analysis on grid, and Gridder, validation, please see Himes et al. (in prep) for a more thorough description.

3.2. Geologically Motivated CH_4 Abundances

We begin by presenting the detectability of CH_4 as a function of SNR for the fiducial modern-Earth case, as examined by S23, BARBIE1, and BARBIE2, to maintain consistency (all CH_4 data and calculated log-Bayes factors across abundance, SNR, and wavelength will be available to the community on Zenodo²). All other parameters were left to modern Earth values, including a modern Earth value of H_2O . However, a modern level of CH_4 (1.65×10^{-6}) is completely undetectable at all SNRs and bandpass widths tested at a resolving power of 140 and 70. Many other works have previously found the same result, due to the low concentration and thus weak absorption features (Schwieterman et al. 2018; Damiano & Hu 2022; Young et al. 2024; Gilbert-Janizek et al. 2024). Since a modern Earth CH_4 was not possible to detect, we quickly proceeded to the varying abundances listed in Table 1 to explore the minimum value at which CH_4 could be detected.

For our abundance case study, we vary the abundance of CH_4 above modern Earth values up to a cap of the Archean Earth value (7.07×10^{-3}). We also vary the SNR for each abundance level to fully investigate the trade-off between higher SNR and molecular detectability. The CH_4 abundances investigated are presented in Table 1, along with intermediate values to fill in the large gap between the Hadean and Archean epochs.

In Figures 5a, 5b, and 5c, we present the strong detectability of the three highest CH_4 abundances in our study, along with a modern H_2O abundance for context, in purple triangles and pink squares respectively. SNR is on the y-axis, with bandpass centers on the x-axis. We see that, as expected, as the abundance of CH_4 increases, the required SNR for detection decreases, with SNRs of 9, 5, and 3 for CH_4 abundances of 4.15×10^{-4} , 1.65×10^{-3} , and 7.07×10^{-3} , respectively. Notably, at 4.15×10^{-4} , the lowest SNR (9) is accessible at $\sim 1.05 \mu\text{m}$, where at 1.65×10^{-3} and 7.07×10^{-3} abundances, the lowest SNRs are accessible at $\sim 0.9 \mu\text{m}$. In order to achieve a detection of CH_4 at 4.15×10^{-4} at 0.9 μm , an SNR of 13 is necessary.

Looking at the full range of abundance values in our study, we present a heat map showing detection strength as a function of SNR (y-axis) and CH_4 abundance (x-axis) in Figure 6a. The color bars represent the range of 0–5 log-Bayes factor, between unconstrained and strong detection. We see here that CH_4 is not strongly detectable until 4.15×10^{-4} (Phanerozoic), at which point an SNR of 9 is required. Moving to higher abundances

² DOI: 10.5281/zenodo.13760695

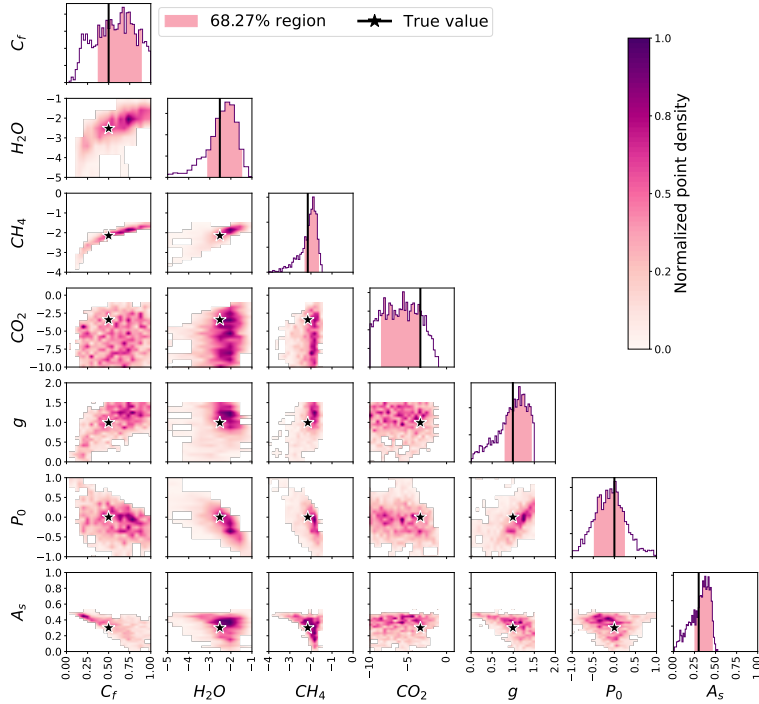
1.1 μm , SNR = 20

Figure 4. Corner plot for Archean CH_4 abundance. The 68% credible regions are shown as pink shading in the 1D marginalized posterior distributions along the diagonal of the corner plot, and the true values are represented by black lines in the diagonals of the corner plot, and black stars within the 2D plots.

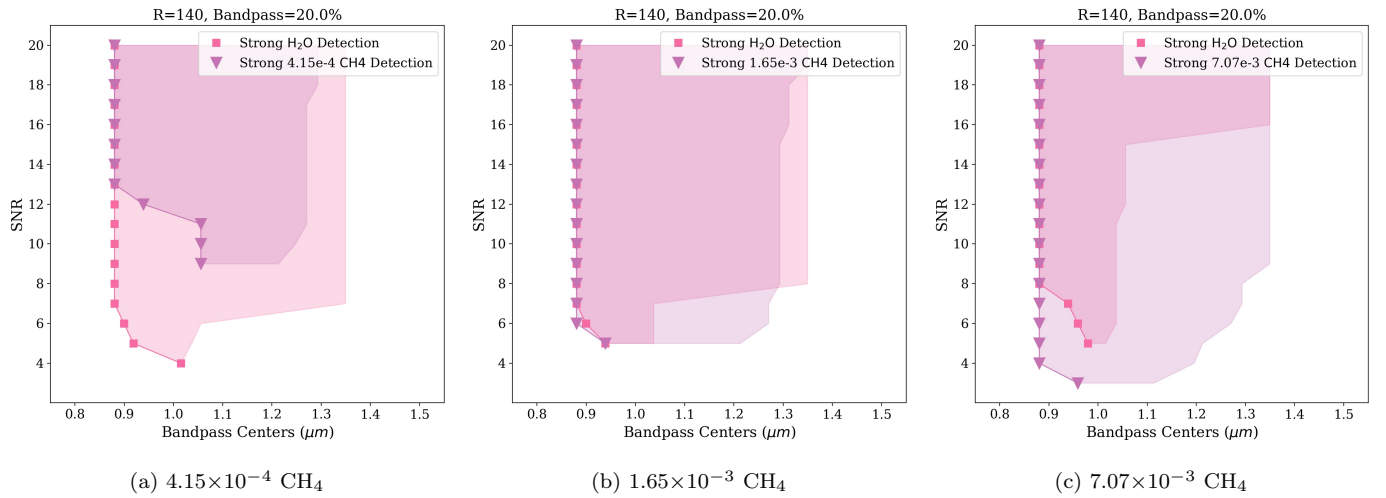


Figure 5. Summary of the bandpasses where CH_4 and H_2O are detectable for 3×10^{-3} (modern) H_2O and varying CH_4 based on Table 1. The shortest bandpass center at which one can achieve a strong detection for H_2O or a strong detection for CH_4 , are shown in pink squares and light purple triangles respectively. SNR is on the y-axis, and the bandpass centers are on the x-axis. We also show the range out to the longest wavelength at which the same detection is achieved as shaded regions.

significantly drops the required SNR for strong detection, with 1.65×10^{-3} (Early Phanerozoic) requiring an SNR of 5 and 7.07×10^{-3} (Archean) detectable at all SNRs. At low abundances, such as a modern Earth

value of 1.65×10^{-6} , CH_4 is not detectable at any SNR. Interestingly, at 1×10^{-4} a weak detection is possible at an SNR of 20, with the next value of 4.15×10^{-4} only requiring an SNR of 9 for strong detection as mentioned,

and an SNR of 6 for weak detection. This results in a very drastic change in CH₄ detection over a relatively small change in abundance of CH₄.

However, returning to Figure 5, we see a significant change in detectability for H₂O across CH₄ abundance. A higher SNR is required to detect H₂O as CH₄ increases. Also as the CH₄ abundance increases, the range of strong H₂O detection as a function of wavelength decreases, with a sharp cut off at $\sim 1.1 \mu\text{m}$. For longer wavelengths than $1.1 \mu\text{m}$, it requires a high SNR (≥ 15) to detect H₂O although there is a very large H₂O feature at $1.35 \mu\text{m}$. This indicates that the H₂O features are being masked by strong CH₄ features, thus H₂O detectability is impacted.

This is confirmed in Figure 7, which presents the spectrum of modern H₂O and three increasing values of CH₄ in three panels (Phanerozoic, Early, and Late Archean from top to bottom) as a function of wavelength and geometric albedo (x-axis and y-axis, respectively). As CH₄ increases in abundance, the absorption feature aligns more closely with that of H₂O, particularly between $\sim 1.1 \mu\text{m}$ and $1.2 \mu\text{m}$. This results in an inflection point, wherein H₂O is more difficult to detect due to the absorption feature being masked by the overpowering CH₄. This led us to investigate the opposite effect - does H₂O mask the detection of CH₄ at lower CH₄ abundance?

We reran all values of CH₄ in Table 1, however we set the abundance of H₂O to zero in our fiducial spectrum. We find that indeed, our detection of CH₄ changes dramatically. In Figure 6b, we again present a detectability heatmap across all abundances of CH₄ as in Figure 6a, although with no H₂O present. We see that CH₄ is strongly detectable down to 7×10^{-5} VMR at an SNR of 14, and 4.15×10^{-4} VMR was detectable at an SNR of 6. Thus, with the absence of H₂O, our detectable CH₄ abundance shifts down over an order of magnitude. We can see the effect of H₂O on CH₄ detectability, and this can suggest that the abundance of CH₄ cannot accurately be determined unless you also separately constrain H₂O abundance. However, we want to further understand the interactions between varying abundances of H₂O and CH₄.

3.3. H₂O and CH₄ Detection Degeneracy

We ran a suite of retrievals with all combined H₂O and CH₄ values shown in Table 2, at 20%, 30%, and 40% bandpass widths - note that these values were selected purely to understand the inflection point of molecular abundance and detectability, with the highest H₂O abundance at modern levels (3×10^{-3} VMR) and the highest CH₄ abundance at Archean levels (7.07×10^{-3} VMR). Our lowest tested value of CH₄ is (1×10^{-4}

VMR), the first abundance at which any detection is possible.

CH ₄ (VMR)	H ₂ O (VMR)
3×10^{-5}	3×10^{-5}
1×10^{-4}	1×10^{-4}
3×10^{-4}	3×10^{-3}
1×10^{-3}	1×10^{-4}
3×10^{-3}	3×10^{-3}
7×10^{-3}	1×10^{-2}

Table 2. All values for CH₄ and H₂O run for our analysis of detectability dependence on molecular abundance. We tested all combinations of abundances, leading to 25 abundance combinations.

In Figure 8, we present the results of our degeneracy study as six heatmaps at $1.1 \mu\text{m}$ and the longest possible bandpass (top and bottom rows, respectively), wherein the color corresponds to the SNR, with the required SNR for strong detection labeled on the plot. The x-axis is the H₂O abundance, the y-axis is CH₄ abundance, with a 20%, 30%, and 40% bandpass width, respectively, in columns. All results are with $R=70$, the current fiducial resolving power in the NIR. We can see as a trend in Figure 8 that the bandpass width has a very large impact on detectability for CH₄ as a function of abundances: at high CH₄ abundances, especially at $1.1 \mu\text{m}$ where there is a large CH₄ absorption feature, Archean levels of CH₄ remain essentially unchanged through bandpass width. This reaffirms our earlier results that high CH₄ did not vary through bandpass width and that H₂O abundance is a large factor in detectability. Looking first to Figures 8a - 8c, at high CH₄ values, 3×10^{-3} VMR and above, the H₂O abundance minimally influences the CH₄ detectability. We begin to see an influence in detectability at 1×10^{-3} VMR, where at the lowest H₂O abundance (3×10^{-5} VMR) the required SNR for CH₄ detection is *sim4*, through the central H₂O abundances, the required SNR is *sim6* for CH₄ detection, and at the highest H₂O abundance (1×10^{-2} VMR), the required SNR for CH₄ detection is up to 11 at a 20% bandpass, and an 8 for a 40% bandpass. The CH₄ abundance is unchanging across this range of H₂O abundances; thus it is clear that the influence must be H₂O. This influence continues to grow stronger as the CH₄ abundance decreases, with 3×10^{-4} VMR CH₄ abundance requiring an SNR of 8 at the lowest H₂O abundances for a 20% bandpass and a 6 for 30% and 40%, and an SNR higher than 20 (i.e., undetectable in our study) at the highest H₂O abundances. The degeneracy is most obvious at 1×10^{-4} VMR CH₄ abundance, with each increas-

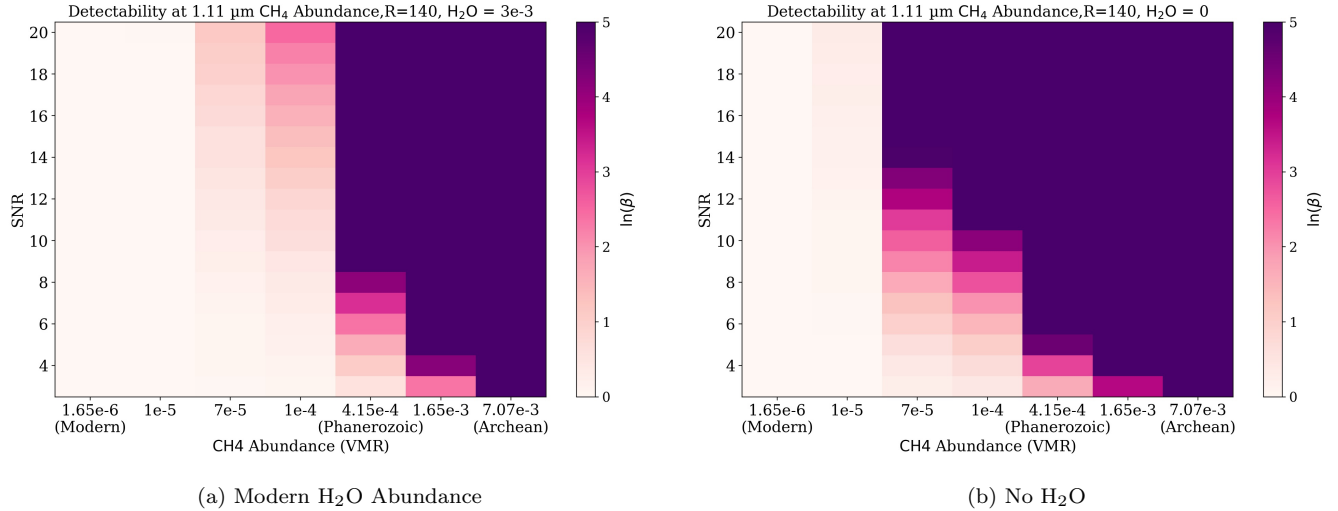


Figure 6. Heatmap plots illustrating detection strength as a function of SNR and varying CH₄ abundance with two H₂O values. SNR is on the y-axis, CH₄ abundance is on the x-axis, and the color bar shows the range of log-Bayes Factor ($\ln B$) from 0 to 5 to describe detection strength. $\ln B < 2.5$ are unconstrained, $2.5 \leq \ln B < 5$ are weak, and $\ln B > 5$ are strong, as in prior figures.

ing abundance of H₂O increasing the required SNR for strong CH₄ detection - and resulting in no detections.

In Figures 8d - 8f, we adjust the wavelength that is being investigated. Since the bandpass centers change as the bandpass width increases, the final bandpass is investigated in 8d - 8f with different bandpass centers. The emphasis in this last bandpass is in the 1.3 μm feature that appears for both CH₄ and H₂O. We find a similar trend to the above, with higher SNR requirements at each bandpass. With the 20% bandpass width (Figure 8d) specifically, the required SNR is higher than in Figures 8a - 8c, especially at high H₂O. In fact, at the highest value of H₂O (1×10^{-2} VMR), CH₄ is not detectable at 3×10^{-3} VMR and 1×10^{-3} VMR although both of those abundances were still detectable at shorter wavelengths. Thus longer wavelengths (e.g. 1.35 μm) are not well suited for CH₄ detection, especially with narrower bandpasses.

Next, we investigate the H₂O detectability. We present in Figure 9 another set of heatmaps to investigate how the detection of H₂O changes as a function of CH₄ abundance. All plot aspects remain the same as Figure 8, with the exception that we are investigating H₂O detectability. We again see that there is a strong correlation with the bandpass width, with detectability increasing as the bandpass width increases, especially at shorter wavelengths. At shorter wavelengths, such as 1.1 μm , H₂O is detectable at all but the lowest abundances, with changing SNR. At a modern-Earth level of H₂O, detectability at a 20% bandpass width requires at most an SNR of 12 and more than halves to an SNR ≤ 5 for a

bandpass width of 40%. However, this does not hold for long wavelengths. We find that at longer wavelengths, the high CH₄ abundances completely mask the H₂O features leading to an inability to detect H₂O at high CH₄ or low H₂O. However, we did find that at low H₂O and sufficiently low CH₄, the presence of both molecules together increases the detectability of H₂O, likely due to the degeneracy between the two molecules being broken in this wavelength regime.

4. DISCUSSION

Understanding the potential for dual detection of atmospheric constituents is an important factor in optimizing the required telescope observing time. Figure 5a shows how crucial this investigation is in the NIR. At the lowest detectable values of CH₄ in our initial investigation, in order to detect both H₂O and CH₄ an SNR of 9 is required at 1.1 μm , and this remains possible out to 1.2 μm . In order to detect both H₂O and low CH₄ at shorter wavelengths, such as at 0.9 μm , an SNR of ≥ 13 is required. This is a significant difference in SNR and would result in a drastic increase in required exposure time. However, the optimal wavelength for a detection of both molecules reverses at higher CH₄ abundances - the detectability of H₂O is impacted at longer wavelengths as shown in Figure 5c. In order to detect both H₂O and CH₄ at 1.1 μm , an SNR of ≥ 15 is required; however, at 0.9 μm the combined detection is accessible at an SNR of 5. We begin to see that there is a relationship between H₂O and CH₄, which is further confirmed by the degeneracy between H₂O and CH₄ shown in Figure 4.

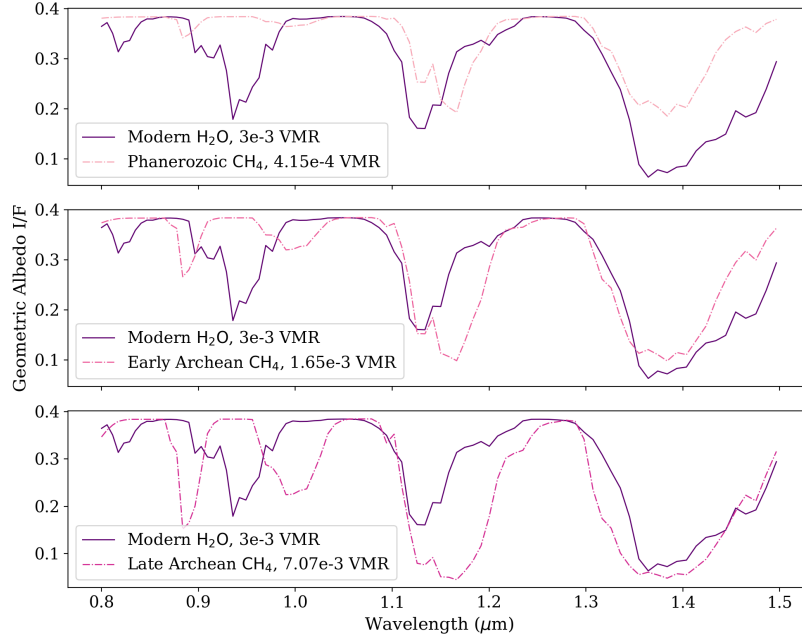


Figure 7. Multi-panel plot illustrating overlap of H₂O and CH₄ features in the NIR wavelength regime. Wavelength is on the x-axis, Geometric Albedo (I/F) is on the y-axis. Each panel shows a modern level of H₂O in dark purple, and a Phanerozoic, Early Archean, and Late Archean abundances of CH₄ in the top, middle, and bottom panels with a dot-dashed shade of pink, respectively.

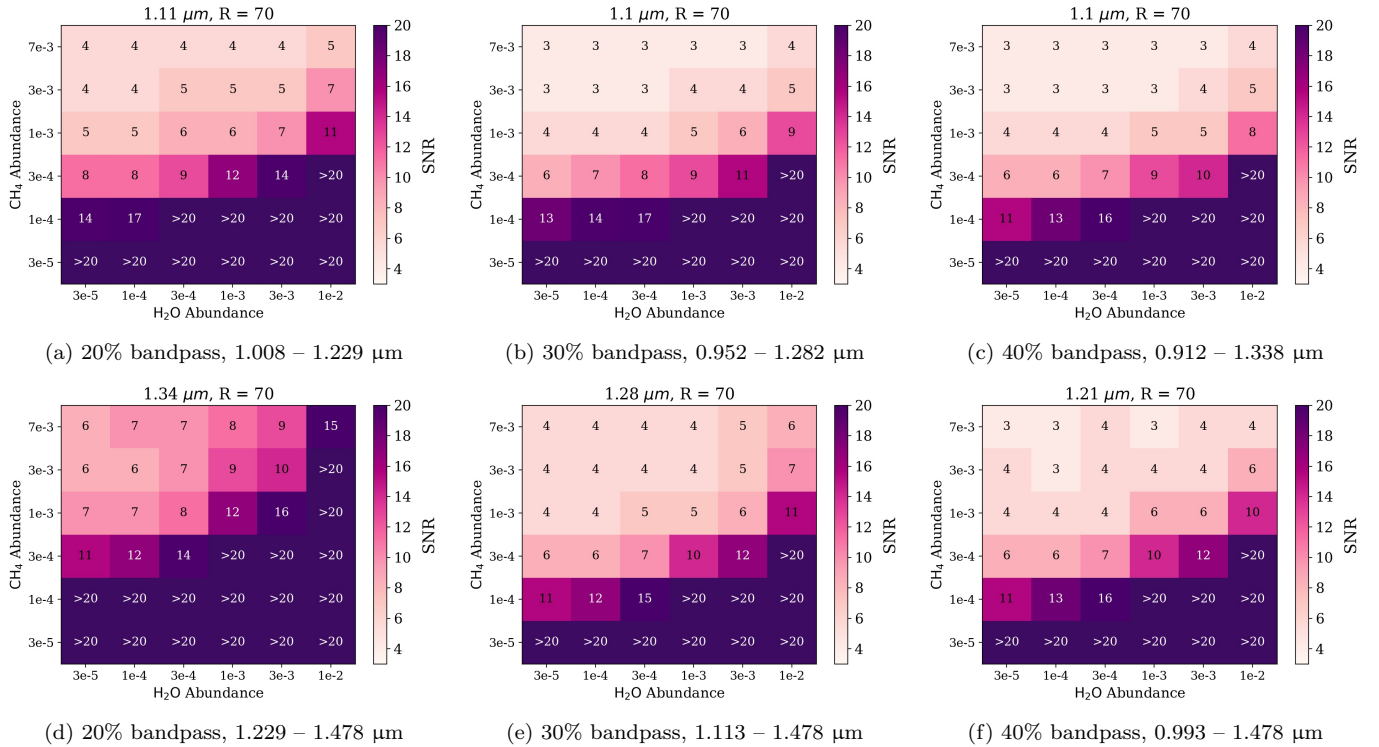


Figure 8. SNRs for Strong CH₄ Detection. Heatmaps of CH₄ detectability as a function of molecular abundance for R = 70, at 1.11 μm (top row) and centered on the 1.3 μm feature (bottom row). We present 20%, 30%, and 40% bandpass widths. y-axis: CH₄ abundance, x-axis: H₂O abundance, heat: SNR. Required SNRs for strong detection are written on the associated block, unless there is no strong detection, thus labeled ‘>20’.

The overlap of molecular absorption features as shown in Figure 7 drives this degeneracy. The bottom most

panel shows both a modern Earth H₂O abundance

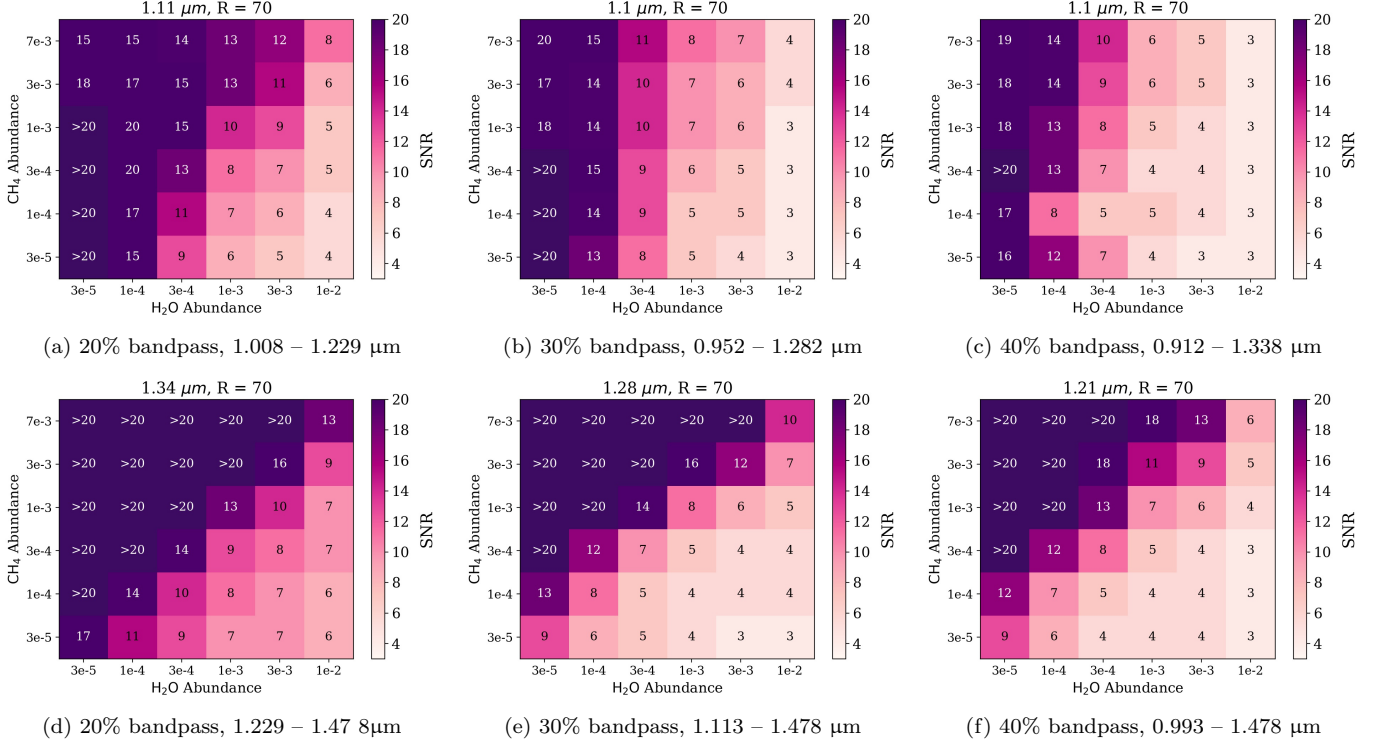


Figure 9. SNRs for Strong H₂O Detection. All plot facets remain the same as Figure 8, but illustrating H₂O detectability.

(3×10^{-3} VMR) and a late Archean Earth CH₄ abundance (7.07×10^{-3} VMR). At $0.9 \mu\text{m}$, we can see the absorption features are orthogonal to each other and thus more easily disentangled. At $1.1 \mu\text{m}$ and longer, the CH₄ feature absorbs much deeper and wider than the H₂O feature, thus completely preventing the possibility of detection without a high SNR. The opposite effect is seen at lower CH₄ abundance, such as the Phanerozoic abundance (4.15×10^{-4} VMR) shown in the top panel of Figure 7. Here, the CH₄ features at $0.9 \mu\text{m}$ are too shallow to be detected without high SNR, and at longer wavelengths (such as $1.4 \mu\text{m}$), the CH₄ feature is completely contained within a much larger H₂O feature and is thus not detectable. At $1.1 \mu\text{m}$, both CH₄ and H₂O are detectable due to the slight offset between the absorption features. We can clearly see that the detectability is a function of the abundance of CH₄ and H₂O, and the abundances of CH₄ and H₂O are degenerate in certain regimes.

To further investigate this degeneracy, we first looked at comparing a null versus modern H₂O value in Figure 6, specifically at $1.1 \mu\text{m}$ where the overlapping features compete. In Figure 6a with modern Earth H₂O abundance, we achieve a strong CH₄ detection at 4.15×10^{-4} VMR at SNR = 9, while still achieving at most a weak detection at 1×10^{-4} . Comparatively, in Figure 6b 4.15×10^{-4} VMR requires an SNR of 6 for

strong detection with no H₂O present, compared to the previous SNR of 9. This confirms that H₂O are degenerate, with detectability reliant on the abundances, and thus we explored a range of abundance values of H₂O and CH₄ to finely understand the relationship we found.

In Figures 8 and 9, we see that there are clear degeneracies between H₂O and CH₄, but with further varying relationships through wavelength. We find that the detectabilities of H₂O and CH₄ are both a function of CH₄ and H₂O abundances, wavelength, and bandpass width. In Figures 8a - 8c and 9a - 9c, we can clearly see that both molecules are far easier to detect, at all bandpass widths, in this wavelength regime when comparing to Figures 8d - 8f and 9d - 9f presenting CH₄ and H₂O at longer wavelengths. At longer wavelengths, both molecules are more difficult to detect, with more abundance values undetectable. Critically, a modern Earth level of H₂O is detectable at all CH₄ abundances and bandpass widths at $1.1 \mu\text{m}$ while it is undetectable at 20% and 30% bandpasses at Archean levels of CH₄ at $1.3 \mu\text{m}$. Similarly, CH₄ is more accessibly detectable across bandwidth at shorter wavelengths, and detectability worsens across the board at longer wavelengths. With this, we can dismiss the possibility of looking for CH₄ and H₂O at the longer wavelengths considered in this study (e.g. $1.35 \mu\text{m} - 1.5 \mu\text{m}$).

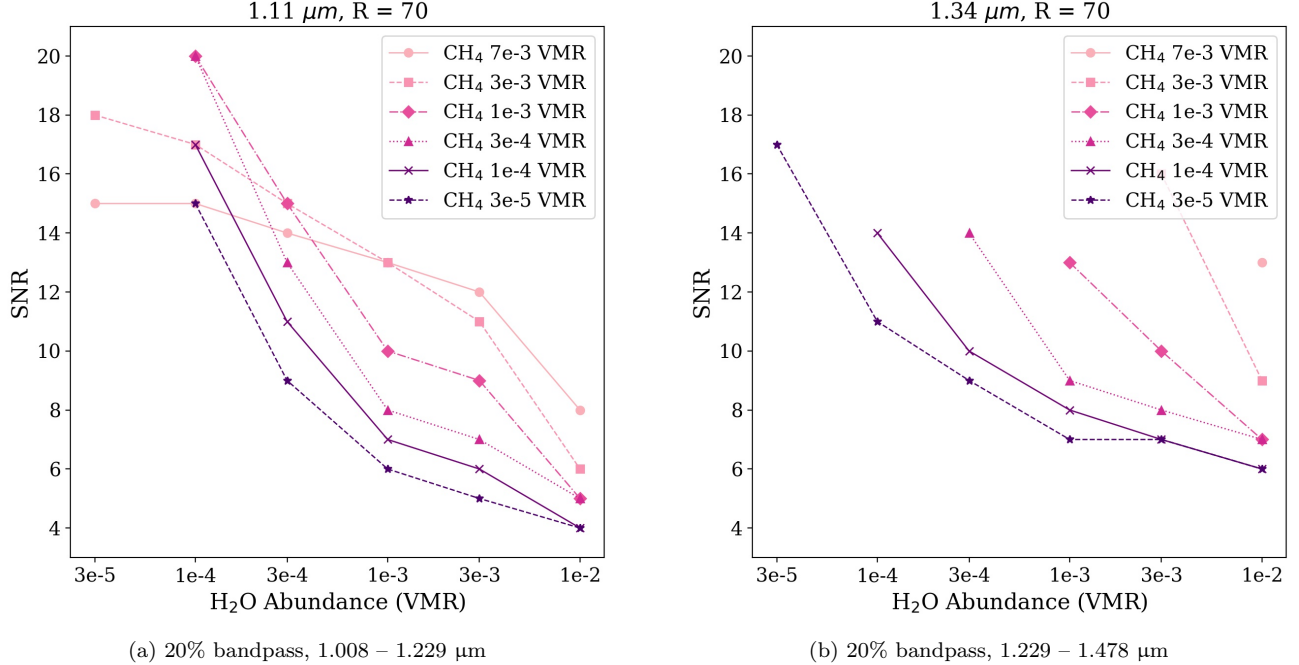


Figure 10. SNRs for Strong H₂O Detection. Plot of the lowest SNR values at which a strong detection is achieved for all H₂O values in our degeneracy investigation at (a) 1.1 μm and (b) 1.34 μm with a 20% bandpass at R=70. The H₂O VMR values are on the x-axis, with SNR on the y-axis. Each line represents a different tested CH₄ value in VMR, labeled in the figure with different line styles and markers.

Focusing on the shorter, 1.1 μm wavelength (i.e., Figures 8a - 8c), we see a steady trend of increased SNR requirements for CH₄ abundances as a function of H₂O abundance. At the Archean abundance, which is of high interest, we see that there is essentially no impact to the CH₄ SNR requirements. However at lower values that can be used as guides for other epochs, such as 3×10^{-4} VMR for the Phanerozoic epoch, we see changes in the required SNR for CH₄ detection. At the lowest H₂O abundance an SNR of 8 is required at a 20% bandpass width, while at the modern H₂O abundance (3×10^{-3} VMR) an SNR of 10 is required - thus the required SNR for detection almost doubles across H₂O abundance ranges, becoming undetectable at higher H₂O abundances. When moving to lower abundances of CH₄ this effect is more pronounced, requiring higher base SNRs at the lowest H₂O abundance and becoming undetectable at mid to high H₂O abundances. This is especially crucial when we consider that, although a modern Earth abundance of CH₄ (1.65×10^{-6} VMR) is not detectable, a high H₂O abundance can mask the detection of CH₄ at low to mid-level values.


Figure 10 shows the CH₄ and H₂O degeneracy in more detail. We present the minimum SNR required per H₂O abundance for H₂O detectability at each CH₄ abundance at R=70 and two wavelengths: 1.1 μm in Figure 10a and 1.34 in Figure 10b. In Figure 10a we can


see that, as before, 3×10^{-5} VMR H₂O is only accessible at the two highest values of CH₄ at 1.1 μm, while otherwise the lowest detectable H₂O abundance is 1×10^{-4} VMR at all other CH₄ values. When moving to longer wavelengths in Figure 10b, the low abundances of H₂O are only accessible at the lowest CH₄ abundances, due to the dual molecular features breaking the spectral degeneracy.


Additionally, although shorter wavelengths are clearly preferred for dual CH₄ and H₂O detection, the 0.9–1.1 μm regime is burdened with increased coronagraph detector noise as detailed below, leading to longer required exposure times and thus higher required SNRs for detection.

5. CONCLUSIONS & FUTURE WORK

To Summarize:

 Modern levels of CH₄ (1.65×10^{-6} VMR) are not detectable at any SNR ≤ 20 with any bandpass width. Archean levels of CH₄ (7.07×10^{-3} VMR) are easily detectable at all SNRs and bandpass widths.

 CH₄ detectability is a function of the abundances of both CH₄ and H₂O, due to the close overlap of spectral features for both species. This overlap between CH₄ and H₂O absorption features becomes most acute at low to moderate CH₄ abundances, and as the H₂O abundance increases, the required SNR for CH₄ detection increases.

 H₂O detectability depends on the abundance of CH₄; as CH₄ abundance increases, the required SNR to detect low to moderate H₂O increases.

CH₄ and H₂O detectability clearly relies heavily on the bandpass selected for observation. At longer wavelengths, detectability drops for both molecules, and instrument efficiency decreases as a result of moving further into the NIR. Shorter wavelengths remain preferable for detection, namely at 1.1 μm for both CH₄ and H₂O, and 0.9 μm for H₂O. However, when searching for moderate to low CH₄ in an H₂O-rich atmosphere, or searching for moderate to low H₂O in a CH₄-rich atmosphere, a higher SNR will be required to disentangle the molecular absorption signals. This may impact the science goals for HWO depending on whether an Archean Earth atmosphere or Modern Earth atmosphere drives the SNR requirement.

In future works, the BARBIE project will culminate with an investigation of molecular detection across the full expected wavelength range for the Habitable

Worlds Observatory. We will explore the requirements for molecular detection across the UV, optical, and NIR to determine the optimal wavelength range and SNR per molecule for strong detection. These metrics will be coupled with also varying the bandpass width across 20%, 30%, and 40% bandpasses, with the new addition of a 10% bandpass width. By using the KEN grids, we will explore molecular relationships through wavelength to investigate the most efficient observing strategy to detect multiple molecules with the most optimal bandpass wavelength, width, and SNR.

We also note that many of the critical wavelength bandpasses for optimal observation of H₂O fall at the intersection of the high-sensitivity regions of different detector technologies. This wavelength dependency could significantly impact the requirements for biosignature detection and result in significant differences to characterization yields, as shown by Stark et al. (2024). In future works, we will investigate how coronagraph detectors and their wavelength-dependent sensitivity can vary the detectability of different molecular species.

N. L. gratefully acknowledges financial support from an NSF GRFP and NASA FINESST. N.L. gratefully acknowledges Dr. Joseph Weingartner for his support and editing. N. L. also gratefully acknowledges Greta Gerwig, Margot Robbie, Ryan Gosling, Emma Mackey, and Mattel Inc.™ for Barbie (doll, movie, and concept), for which this project is named after. This Barbie is an astrophysicist! The authors would like to thank the Sellers Exoplanet Environments Collaboration (SEEC) and ExoSpec teams at NASA's Goddard Space Flight Center for their consistent support. MDH was supported in part by an appointment to the NASA Postdoctoral Program at the NASA Goddard Space Flight Center, administered by Oak Ridge Associated Universities under contract with NASA.

REFERENCES

- Arney, G., Domagal-Goldman, S. D., Meadows, V. S., et al. 2016, *Astrobiology*, 16, 873, doi: [10.1089/ast.2015.1422](https://doi.org/10.1089/ast.2015.1422)
- Benneke, B., & Seager, S. 2013, *ApJ*, 778, 153, doi: [10.1088/0004-637X/778/2/153](https://doi.org/10.1088/0004-637X/778/2/153)
- Buchner, J. 2016, *Statistics and Computing*, 26, 383, doi: [10.1007/s11222-014-9512-y](https://doi.org/10.1007/s11222-014-9512-y)
- . 2019, *PASP*, 131, 108005, doi: [10.1088/1538-3873/aae7fc](https://doi.org/10.1088/1538-3873/aae7fc)
- . 2021, *The Journal of Open Source Software*, 6, 3001, doi: [10.21105/joss.03001](https://doi.org/10.21105/joss.03001)
- Cobb, A. D., Himes, M. D., Soboczenski, F., et al. 2019, *AJ*, 158, 33, doi: [10.3847/1538-3881/ab2390](https://doi.org/10.3847/1538-3881/ab2390)
- Damiano, M., & Hu, R. 2022, *AJ*, 163, 299, doi: [10.3847/1538-3881/ac6b97](https://doi.org/10.3847/1538-3881/ac6b97)
- Damiano, M., Hu, R., & Mennesson, B. 2023, *AJ*, 166, 157, doi: [10.3847/1538-3881/acefd3](https://doi.org/10.3847/1538-3881/acefd3)
- Domagal-Goldman, S. D., Segura, A., Claire, M. W., Robinson, T. D., & Meadows, V. S. 2014, *ApJ*, 792, 90, doi: [10.1088/0004-637X/792/2/90](https://doi.org/10.1088/0004-637X/792/2/90)

- Feng, Y. K., Robinson, T. D., Fortney, J. J., et al. 2018, *AJ*, 155, 200, doi: [10.3847/1538-3881/aab95c](https://doi.org/10.3847/1538-3881/aab95c)
- Feroz, F., Hobson, M. P., & Bridges, M. 2009, *MNRAS*, 398, 1601, doi: [10.1111/j.1365-2966.2009.14548.x](https://doi.org/10.1111/j.1365-2966.2009.14548.x)
- Fisher, C., Hoeijmakers, H. J., Kitzmann, D., et al. 2020, *AJ*, 159, 192, doi: [10.3847/1538-3881/ab7a92](https://doi.org/10.3847/1538-3881/ab7a92)
- Gilbert-Janizek, S., Meadows, V. S., & Lustig-Yaeger, J. 2024, *PSJ*, 5, 148, doi: [10.3847/PSJ/ad381e](https://doi.org/10.3847/PSJ/ad381e)
- Harrington, J., Himes, M. D., Cubillos, P. E., et al. 2022, *PSJ*, 3, 80, doi: [10.3847/PSJ/ac3513](https://doi.org/10.3847/PSJ/ac3513)
- Himes, M. D., Mandell, A. M., & Latouf, N. in prep
- Himes, M. D., Harrington, J., Cobb, A. D., et al. 2022, *PSJ*, 3, 91, doi: [10.3847/PSJ/abe3fd](https://doi.org/10.3847/PSJ/abe3fd)
- Juanola-Parramon, R., Zimmerman, N. T., Pueyo, L., et al. 2022, *Journal of Astronomical Telescopes, Instruments, and Systems*, 8, 034001, doi: [10.1117/1.JATIS.8.3.034001](https://doi.org/10.1117/1.JATIS.8.3.034001)
- Kaltenegger, L., Traub, W. A., & Jucks, K. W. 2007, *ApJ*, 658, 598, doi: [10.1086/510996](https://doi.org/10.1086/510996)
- Kasting, J. 2005, *Precambrian Research*, 137, 119, doi: [10.1016/j.precamres.2005.03.002](https://doi.org/10.1016/j.precamres.2005.03.002)
- Krissansen-Totton, J., Olson, S., & Catling, D. C. 2018, *Science Advances*, 4, eaao5747, doi: [10.1126/sciadv.aao5747](https://doi.org/10.1126/sciadv.aao5747)
- Latouf, N., Mandell, A. M., Villanueva, G. L., et al. 2023, *AJ*, 166, 129, doi: [10.3847/1538-3881/acebc3](https://doi.org/10.3847/1538-3881/acebc3)
- . 2024, *AJ*, 167, 27, doi: [10.3847/1538-3881/ad0fde](https://doi.org/10.3847/1538-3881/ad0fde)
- Line, M. R. 2013, *The Astrophysical Journal*, 775, doi: [10.1088/0004-637X/775/2/137](https://doi.org/10.1088/0004-637X/775/2/137)
- Lupu, R. E., Marley, M. S., Lewis, N., et al. 2016, *AJ*, 152, 217, doi: [10.3847/0004-6256/152/6/217](https://doi.org/10.3847/0004-6256/152/6/217)
- Márquez-Neila, P., Fisher, C., Sznitman, R., & Heng, K. 2018, *Nature Astronomy*, 2, 719, doi: [10.1038/s41550-018-0504-2](https://doi.org/10.1038/s41550-018-0504-2)
- National Academies of Sciences, Engineering, and Medicine. 2021, *Pathways to Discovery in Astronomy and Astrophysics for the 2020s*, doi: [10.17226/26141](https://doi.org/10.17226/26141)
- Nayak, M., Lupu, R., Marley, M. S., et al. 2017, *PASP*, 129, 034401, doi: [10.1088/1538-3873/129/973/034401](https://doi.org/10.1088/1538-3873/129/973/034401)
- Planavsky, N. J., Reinhard, C. T., Wang, X., et al. 2014, *Science*, 346, 635, doi: [10.1126/science.1258410](https://doi.org/10.1126/science.1258410)
- Por, E. H. 2020, *ApJ*, 888, 127, doi: [10.3847/1538-4357/ab3857](https://doi.org/10.3847/1538-4357/ab3857)
- Robinson, T. D., & Salvador, A. 2023, *PSJ*, 4, 10, doi: [10.3847/PSJ/acac9a](https://doi.org/10.3847/PSJ/acac9a)
- Ruane, G. J., Huby, E., Absil, O., et al. 2015, *A&A*, 583, A81, doi: [10.1051/0004-6361/201526561](https://doi.org/10.1051/0004-6361/201526561)
- Schindler, T. L., & Kasting, J. F. 2000, *Icarus*, 145, 262, doi: [10.1006/icar.2000.6340](https://doi.org/10.1006/icar.2000.6340)
- Schwieterman, E. W., Kiang, N. Y., Parenteau, M. N., et al. 2018, *Astrobiology*, 18, 663, doi: [10.1089/ast.2017.1729](https://doi.org/10.1089/ast.2017.1729)
- Smith, A. J. R. W., Feng, Y. K., Fortney, J. J., et al. 2020, *AJ*, 159, 36, doi: [10.3847/1538-3881/ab5a8a](https://doi.org/10.3847/1538-3881/ab5a8a)
- Stark, C. C., Mennesson, B., Bryson, S., et al. 2024, arXiv e-prints, arXiv:2405.19418, doi: [10.48550/arXiv.2405.19418](https://doi.org/10.48550/arXiv.2405.19418)
- Susemihl, N., Mandell, A. M., Villanueva, G. L., et al. 2023, *AJ*, 166, 86, doi: [10.3847/1538-3881/ace43b](https://doi.org/10.3847/1538-3881/ace43b)
- The LUVOIR Team. 2019, arXiv e-prints, arXiv:1912.06219. <https://arxiv.org/abs/1912.06219>
- Villanueva, G. L., Liuzzi, G., Faggi, S., et al. 2022, *Fundamentals of the Planetary Spectrum Generator (Self-Published)*
- Villanueva, G. L., Smith, M. D., Protopapa, S., Faggi, S., & Mandell, A. M. 2018, *JQSRT*, 217, 86, doi: [10.1016/j.jqsrt.2018.05.023](https://doi.org/10.1016/j.jqsrt.2018.05.023)
- Wogan, N., Krissansen-Totton, J., & Catling, D. C. 2020, *PSJ*, 1, 58, doi: [10.3847/PSJ/abb99e](https://doi.org/10.3847/PSJ/abb99e)
- Young, A. V., Crouse, J., Arney, G., et al. 2024, *PSJ*, 5, 7, doi: [10.3847/PSJ/ad09b1](https://doi.org/10.3847/PSJ/ad09b1)
- Zingales, T., & Waldmann, I. P. 2018, *AJ*, 156, 268, doi: [10.3847/1538-3881/aae77c](https://doi.org/10.3847/1538-3881/aae77c)